Stromboli volcano (Aeolian Archipelago, Italy): An open window on the deep-feeding system of a steady state basaltic volcano

A. Bertagnini,[1] N. Métrich,[2] P. Landi,[1] and M. Rosi[3]

Received 9 August 2002; revised 18 February 2003; accepted 18 March 2003; published 12 July 2003.

[1] Paroxysms at Stromboli are the most violent manifestations of the persistent activity and are related to the emission of small volumes (10^3–10^5 m^3) of nearly aphyric HK-basaltic pumices. They offer the exceptional opportunity to detail the mixing-crystallization-degassing processes that occur in a steady state basaltic arc volcano. We present mineralogy, major, volatile, and trace element geochemistry of olivine-hosted melt inclusions of these pumices. In all the paroxysms, melt inclusions hosted in olivines Fo_{88-91} have recorded the parental melts rich in CaO (up to 14.5 wt %) but low in FeO (6–7 wt %). They demonstrate recurrent variations in the K_2O content (1.6–1.3 wt %) and S/Cl ratios (1.2–0.8) of the melts that entered the deep system. Dynamic magma mixing between melts slightly distinct by their degree of evolution, rapid crystallization, and entrapment of gas-oversaturated melts during decompression are indicated by (1) the high density of irregular, clear melt inclusions, and embayments in homogeneous olivines ($Fo_{87\pm0.5}$–$Fo_{83\pm0.5}$), (2) the variable ratio between melt and gas bubble, and (3) the variability of melt inclusion compositions in both major (CaO/Al_2O_3 = 1–0.59) and volatile (3.4–1.8 wt % H_2O, 1582–1017 ppm CO_2) elements. FeO-rich melt inclusions in patchy, reversely zoned olivines also demonstrate interactions between ascending melt blobs and inherited olivine crystals. We propose a model involving a vertically extended dike-like system, where magmas progress and differentiate. On the basis of olivine growth rate calculations the volatile-rich magma blobs may ascend within few hours to few tenths of hours. Finally, we propose that sulfur degassing is possibly initiated during the early stage of magma differentiation. *INDEX TERMS:* 1010 Geochemistry: Chemical evolution; 3620 Mineralogy, Petrology, and Mineral Physics: Crystal chemistry; 3655 Mineralogy, Petrology, and Mineral Physics: Major element composition; 8434 Volcanology: Magma migration; 8439 Volcanology: Physics and chemistry of magma bodies; *KEYWORDS:* Stromboli, basaltic pumice, olivine, melt inclusions, volatiles, sulfur degassing, growth rate

Citation: Bertagnini, A., N. Métrich, P. Landi, and M. Rosi, Stromboli volcano (Aeolian Archipelago, Italy): An open window on the deep-feeding system of a steady state basaltic volcano, *J. Geophys. Res.*, *108*(B7), 2336, doi:10.1029/2002JB002146, 2003.

1. Introduction

[2] Stromboli, the northernmost volcano island of the Aeolian Archipelago in southern Italy raises 924 m above sea level (asl) but represents the emergent part of a large 2500-m-high stratovolcano. The active vents are located in a flattish area (the Crater Terrace) at about 750 m asl in the upper part of a horseshoe-shaped structure (the Sciara del Fuoco) which represents the scar of several flank collapses [*Tibaldi*, 2000]. The volcano is famous for its exceptionally persistent activity that started after a period dated between the 3rd and the 7th centuries A.D. and has continued until now without interruptions and modifications in eruptive style [*Rosi et al.*, 2000]. Persistent activity consists of continuous degassing (6000–12,000 t d^{-1} H_2O, CO_2, SO_2, HCl, and HF [*Allard et al.*, 1994]), mild intermittent explosions (normal Strombolian activity), rare lava emissions and sporadic more violent explosions (so-called major explosions and paroxysms [*Barberi et al.*, 1993]).

[3] The mild intermittent explosions yield gas jets, each 10–20 min, and throw out scoriae, lava lumps, ash and blocks up to heights of a few tens to hundreds of meters, which fall in the vicinity of the craters. They tap a crystal-rich and degassed magma which resides within the upper part of the plumbing system [*Bertagnini et al.*, 1999; *Métrich et al.*, 2001]. As a result, typical products are dark, low-vesicular scoriae rich (~50 vol %) in millimeter-sized crystals of plagioclase, pyroxene, and olivine. Every 10–20 years in the past two centuries the volcano has produced outpouring of lavas which have flowed onto the Sciara del Fuoco slope. Lavas are also highly porphyritic with the same crystal content and mineralogy of the crystal-rich scoriae.

[4] Major explosions eject meter-sized bombs and blocks within a distance of several hundreds of meters from the

[1]Istituto Nazionale di Geofisica e Vulcanologia, Sezione Roma I sede di Pisa, Pisa, Italy.
[2]Laboratoire Pierre Süe, CEA-CNRS, Gif sur Yvette, France.
[3]Dipartimento di Scienze della Terra, Universita' degli Studi di Pisa, Pisa, Italy.

0148-0227/03/2002JB002146$09.00

craters. Showers of ash and lapilli can fall on the slopes of the volcano. These events consist either of one discrete explosion or of several explosions usually from different vents, at intervals of a few seconds to tens of minutes. On average, the reported major explosions have been of 1–2 events yr^{-1} over the past 110 years. Paroxysms are less frequent, the last ones happened in 1930 and 1944, and represent the most powerful and damaging eruptive manifestations of the volcano. They usually last from several hours to a few days, and consist of violent explosions often accompanied by strong detonations heard at distances of over 80 km. During such episodes, showers of incandescent scoriae and bombs, and meter-sized ballistic lithic blocks fall within a distance of several kilometers from the craters, eventually reaching the two villages, Stromboli and Ginostra, located on the coast. The lapilli fallout leads to the accumulation of discrete, centimeter-thick tephra beds. Both, major explosions and paroxysms are related to the ascent and violent emission of volatile-rich magma blobs emitted as nearly aphyric golden pumices together with crystal-rich scoriae and bombs identical to those of the normal activity [*Barberi et al.*, 1993; *Bonaccorso et al.*, 1996; *Bertagnini et al.*, 1999; *Coltelli et al.*, 1999; *Francalanci et al.*, 1999; *Métrich et al.*, 2001]. A rough estimate of the volume of golden pumice gives maximum values of 10^3–10^5 m^3. The volume of emitted products, both juvenile and lithic clasts, is low probably less than 10^6 m^3 in the most energetic events. Despite their very different crystal content, both scoria and pumice display closely similar chemical composition between HK-basalts and shoshonitic basalts (according to the classification diagram of *Peccerillo and Taylor* [1976]).

[5] In a previous work, we developed a model dealing with the key role of water at the origin of the crystal-rich magma, which sustains the normal Strombolian activity, and proposed that it results from the low-pressure ''in situ'' crystallization of volatile-rich magma batches through decompression and water exsolution. We also demonstrated that the pumice clasts made of highly vesiculated glass and a few crystals, still record the fingerprint of their parental magmas as melt (glass) inclusions (MI) in olivine grains [*Métrich et al.*, 2001]. They provide the rare occasion to catch a quenched deep-seated, basaltic arc magma.

[6] In the present work, we focus on these pumices to get precise knowledge of the composition of the parental magmas and mechanisms of crystallization and degassing prior to the emission of volatile-rich magma blobs at the origin of the paroxysmal events. In order to do that, we selected new samples emplaced during paroxysms and constituted a complete and detailed data set on 400 MI and their host olivines, combining present and previous results [*Métrich et al.*, 2001]. They reveal a large chemical heterogeneity at the μm scale and indicate different crystallization and cooling histories. On the basis of the morphology and composition of MI and their host crystals we have deciphered the effects of heritage and reequilibration between melts and olivine against that of the equilibrium crystallization and undercooling. We bring new data on the dissolved volatile concentrations and the fluid (CO_2 + H_2O) pressures. The possible residence time of magmas in the conduits is evaluated on the basis of diffusion profiles in olivine and their ascent time deduced from crystal growth rate. Understanding the deep feeding system at Stromboli is a prerequisite for volcanic forecasting.

2. Location and Brief Description of Samples

[7] Two golden pumice samples (St81, St207) were selected and analyzed with respect to their mineralogy together with major and trace element geochemistry in both whole rocks and olivine hosted melt inclusions. They were collected from tephra layers related to paroxysmal eruptions younger than the 3rd through the 7th centuries A.D. [*Rosi et al.*, 2000]. The St81 pumices were sampled from a 3-cm-thick bed, which is the lowest tephra layer encountered by a stratigraphic trench dug at about 500 m asl on the NE flank of the volcano (Trench 2 of *Rosi et al.* [2000]). Two tephra layers in the same trench (St79 intermediate and St82 the youngest) were previously analyzed [*Métrich et al.*, 2001]. All together, the three samples provide a suitable sequence to study the different processes at the origin of the pumice and the paroxysmal events. The St207 sample was recovered from an outcrop at about 150 m asl uphill the village of Stromboli. The St207 pumices represent the lapilli and bombs basal layer of a ~15-cm-thick pumice and ash fallout sequence emplaced during a paroxysmal eruption. Although its stratigraphic position is not well constrained, the St207 pumice was selected because the grain size and the relatively large dispersal of the products suggest that this paroxysmal event was one of the most energetic of the recent eruptions of the volcano. This feature is particularly interesting since we think, on the basis of the previous work, that the most energetic events are able to bring to surface instructive records of the deep feeding system and the most primitive olivine.

[8] The St81 and St207 pumices belong to the HK-basalt field and are analogous to pumices emitted during both paroxysms and major explosions (e.g., August 1998 and August 1999, Table 1). Their crystal content is nearly 10 vol.%, but most of the crystals are inherited from the crystal-rich body, as previously described for the golden pumices emitted during major and paroxymal explosions [*Bertagnini et al.*, 1999; *Rosi et al.*, 2000; *Métrich et al.*, 2001].

3. Microanalyses of Crystals, Melt Inclusions, and Matrix Glasses

[9] Olivines were analyzed and mapped with a Philips XL30 scanning electron microscope equipped with EDAX DX 4 (Dipartimento Scienze della Terra, Pisa, Italy). Compositional profiles were also performed with 5–10 μm steps in order to evaluate the zoning patterns of the crystals.

[10] Melt inclusions and embayments together with glass adhering to the crystals (rim glass) and matrix glasses were analyzed for major elements, Cl, S, using a SX50 CAMECA electron microprobe (Service Camparis, Paris VI). The analytical conditions for glasses were 10 nA beam current, 10 μm beam size, 10–15 s counting time for major elements and 30 nA, 15 μm and 120 s for Cl, S and P. Reproducibility and accuracy of analyses were checked for S and Cl on Alv981 (S = 1110 ± 110 ppm), and VG2 (Cl = 300 ± 35 ppm; S = 1430 ± 60 ppm) basaltic glasses [*Métrich et al.*, 2001]. The compositions of selected Mg-rich olivines and associated spinels were also analyzed at 40

Table 1. Whole Rock Composition of Pumices of Paroxysms and Major Explosions[a]

Sample	St81[b]	St79[b]	St82[b]	St207[b]	St140[b]	St178
SiO_2	51.61	51.51	50.87	51.17	49.05	50.01
TiO_2	0.87	0.87	0.9	0.94	0.97	0.97
Al_2O_3	16.22	16.67	16.56	16.81	17.14	17.14
Fe_2O_3	3.01	3.01	3.46	3.05	4.6	2.56
FeO	5.4	5.10	5.11	5.22	4.4	6.16
MnO	0.16	0.15	0.16	0.16	0.16	0.16
MgO	6.64	6.34	6.66	6.12	6.93	6.37
CaO	10.61	10.34	10.91	10.63	11.59	11.24
Na_2O	2.45	2.75	2.39	2.59	2.38	2.51
K_2O	1.87	2.21	1.82	2.02	1.62	1.75
P_2O_5	0.38	0.39	0.4	0.51	0.42	0.46
H_2O	0.79	0.66	0.77	0.71	0.73	0.60
CaO/Al_2O_3	0.65	0.62	0.66	0.63	0.68	0.66
K_2O/Na_2O	0.76	0.80	0.76	0.78	0.68	0.70
V	247	249	270	251	278	259
Cr	98	132	116	74	51	36
Co	32	31	34	30	34	33
Ni	44	49	51	38	46	37
Rb	63	73	62	64	52	55
Sr	728	756	742	632	701	721
Y	24	25	24	23	26	25
Zr	146	164	148	157	132	141
Nb	18	20	18	16	16	15
Mo	1.51	1.83	1.66	1.33	1.18	1.02
Cs	4.4	5.5	4.6	4.2	3.7	3.5
Ba	954	982	901	902	816	848
La	49	47	45	42	39	42
Ce	96	92	88	84	81	84
Pr	11.3	10.6	10.5	10.1	9.8	9.9
Nd	42	42	40	40	39	39
Sm	8.5	8.2	7.5	8.0	7.8	7.9
Eu	2.2	2.1	2.0	2.1	2.0	2.2
Gd	6.2	6.3	6.3	6.3	6.7	6.4
Tb	0.90	0.84	0.84	0.88	0.95	0.92
Dy	4.72	4.63	4.56	4.60	4.90	4.88
Ho	0.88	0.83	0.87	0.87	0.92	0.88
Er	2.45	2.24	2.19	2.29	2.44	2.21
Tm	0.31	0.34	0.32	0.33	0.36	0.30
Yb	2.36	2.07	2.11	2.16	2.10	2.19
Lu	0.35	0.31	0.29	0.38	0.31	0.31
Hf	3.5	3.4	3.1	3.9	3.2	3.2
Ta	1.22	1.22	1.07	1.16	0.90	1.03
Pb	18	18	16	18	14	14
Th	15.0	18.2	15.6	13.8	11.4	11.9
U	3.91	4.13	3.45	3.59	2.88	2.96

[a]Major elements (in wt %) analyzed by X-ray fluorescence, except for MgO, Na_2O and K_2O analyzed by AAS and FeO by titration. Trace elements (in ppm) analyzed by ICP-MS at Dip.to di Scienze della Terra (Pisa-Italy) (St140) and at CRPG (Nancy-France) (St81, St79, St82, St207, St178).

[b]From *Métrich et al.* [2001]. St 140, major explosion of 23 August 1998, St 178 major explosion of 26 August 1999.

nA, 100–140 s counting time for Ni, Ca, and Mn. Carbon and water in double face-polished MI were determined by Fourier Transform Infrared Spectroscopy using a Nicolet Magna-IR 550 spectrometer, equipped with a Globar source, a MCT/A detector cooled with liquid N_2, a X-KBr beam splitter, and coupled with a Spectra-Tech microscope (Pierre Süe Laboratory, Saclay). The concentrations of total water (H_2O_{mol} + OH^-) and carbon as carbonate were determined using the bands at 3535 cm^{-1} and 1515 cm^{-1}, respectively. They were calculated according to Beer-Lambert's law: $C = 100AM/[\epsilon\rho e]$, where A is the absorbance, M is the molar mass (g mol^{-1}) of the volatile species, ϵ is the molar absorptivity (ϵ^{3535} = 65.7 L mol^{-1} cm^{-1} for water; and $\epsilon^{1515} = 451 - 342$ [Na/(Ca + Na)] for CO_3^{2-} according to *Dixon and Pan* [1995]), e is the thickness (cm), and ρ is the glass density (2.69 g cm^{-3}). The whole procedure is detailed by *Métrich et al.* [2001].

[11] SIMS analyses were performed with a Cameca IMS 4f (at CNR, Istituto di Geoscienze e Georisorse, sezione di Pavia) on spots of 15–20 μm diameter. Quantification was done by an empirical calibration on a number of well-characterized natural minerals (amphiboles and clinopyroxenes) and using ^{30}Si as internal standard. The primary beam consisted of mass analyzed $^{16}O^-$. Analytical conditions were typically 10 nA beam current and 17 keV total impact energy. The ions sputtered from polished, gold coated, samples were transferred to the mass spectrometer by the 25 μm optics and energy filtered by applying −100 V offset voltage, with an energy bandwidth by ±25 eV. Further details on the analytical and quantification procedures are reported by *Bottazzi et al.* [1994]. Estimated accuracy is better than ±10% for element concentration at the ppm level.

4. Olivine and Their Melt Inclusions

[12] About 280 olivine grains were hand-picked from 0.25 to 1 mm grain sizes and 76 were analyzed with SEM. They are usually tabular and nearly euhedral. They show curvilinear lobes and embayments created when crystal is growing as skeletal entity (Figure 1a) or "composed" crystal ensuing from the association of two or more growing nuclei (Figure 1b). The general characteristic of the olivine grains from Stromboli pumice is their huge amount of trapped glass. They also display a large compositional diversity (Fo_{68-89} in ST81; Fo_{67-91} in ST207), but the composition in equilibrium with the whole rocks and matrix glasses belongs to a very narrow range Fo_{86-85}. In both samples two main populations of crystals have been clearly identified on the basis of their compositions and the morphology of their MI.

[13] The first one consists of rare primitive olivines Fo_{88-89} in St81 and Fo_{88-91} in St207. All of them are normally zoned with Fo_{85-86} rim and contain clear glass inclusions associated with Cr-spinel (Cr # 64–67, Mg #59–67) in St207 sample (Figure 1c). The Cr, Al-rich diopside was sporadically found as daughter phase in MI associated with Cr-spinel in olivine Fo_{88}. More evolved, homogeneous olivines with compositions between $Fo_{87\pm0.5}$ and $Fo_{83\pm0.5}$ are dominant. All of them display a constant rim composition Fo_{85-86}. They hold a high density of clear glass trapped as embayments and irregular, elongated inclusions, whose size varies from 10–20 to ~80 μm (Figure 1d). Time was not sufficient to mould regular cavities with "negative crystal shapes" and to create typical primary glass inclusions [*Roedder*, 1984]. The high density of glass embayments and inclusions and the variable proportions between bubble and glass attest to very rapid growth rates of their host from a heterogeneous gas-melt mixture.

[14] The second group comprises crystals with highly variable reverse zoning. Rare olivines show a concentric zoning with core Fo_{80}, homogeneous intermediate zone Fo_{89} and a rim Fo_{86-87}, successively (Figure 1e). However, systematic backscattered electron mappings reveal that in most olivines, the reverse zoning is only preserved as residual patches with Fe-rich composition, randomly distributed in crystal (Figure 1f). As a whole, the olivines

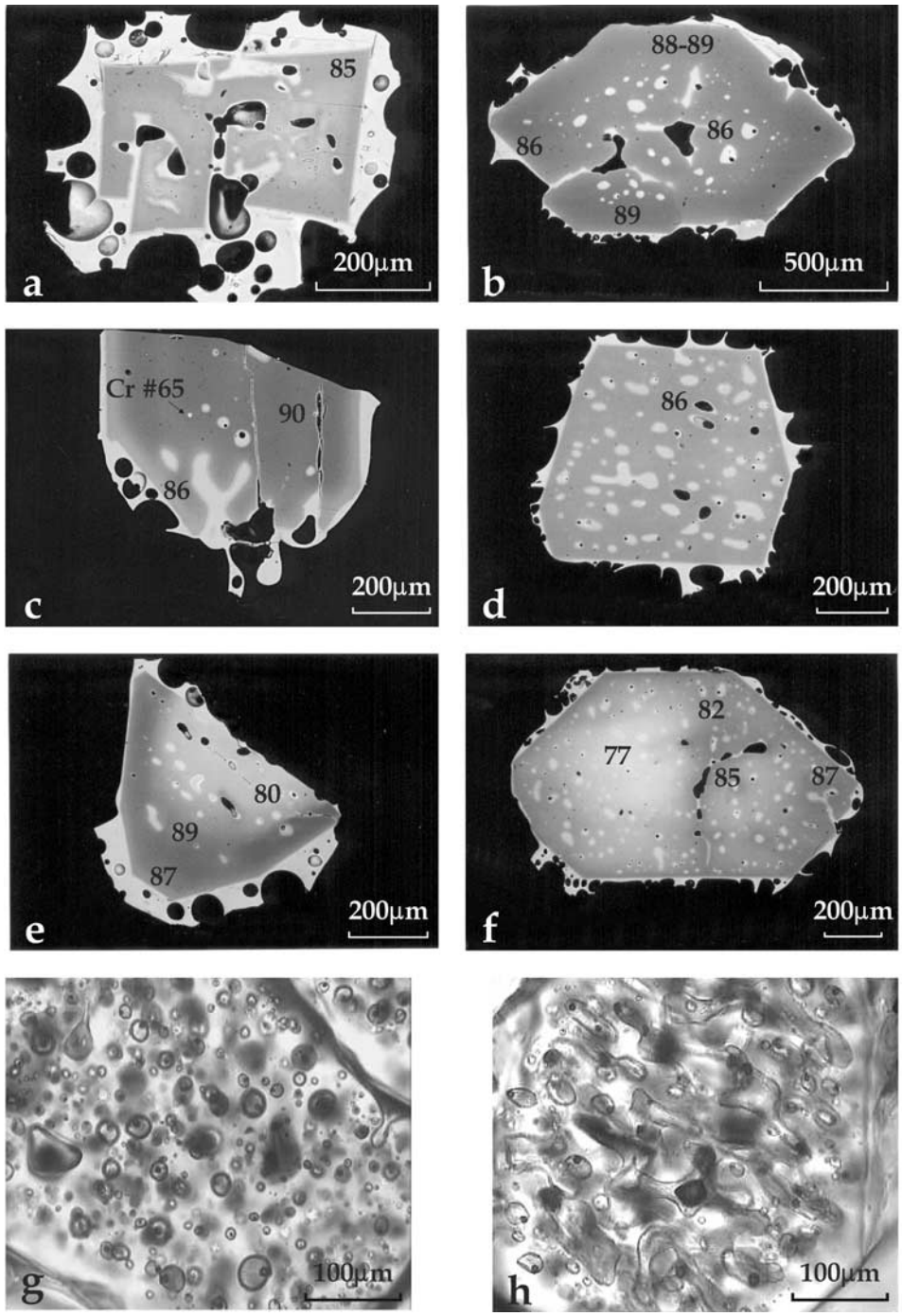

Figure 1. Figures 1a–1f are backscattered electron micrographs of olivines from pumice; the number represents Fo mol % content; darker shading of olivine corresponds to higher Fo content. (a) Skeletal crystal with homogeneous composition (St207 ol a4); (b) ''composed'' nearly euhedral crystal resulting from the association of two or more growing nuclei (St81 ol11); (c) primitive normal-zoned crystal with a Cr-spinel inclusion (St207 ol a5); (d) homogeneous euhedral crystal showing high density of irregular melt inclusions (St81 ol14); (e) zoned crystal with a Fe-rich core surrounded by an intermediate Mg-rich zone and a rim in equilibrium with the matrix glass (St207 ol n13); (f) mottled crystal with residual patches of Fe-rich composition (St81 ol16). Figures 1g and 1h are transmitted light micrographs of melt inclusions. (g) Brownish melt inclusions in reverse-zoned and mottled crystals. This type of melt inclusions is related to dissolution-crystallization processes (St81 ol18). (h) Clear irregular melt inclusions in homogenous crystals. The variable proportion between bubbles and glass indicates heterogeneous trapping of melt and associated gas-rich phase (St81 ol14).

Table 2. Selected Analyses of Melt Inclusions and Rim Glasses

	St81					St207							St82p[b]		St79p[b]	
	Ol 11[a] Mean	Ol 1 MI 1	Ol 8 MI 1	Ol13 Rim Glass	Ol n56 Rim Glass	Ol n13 MI 2	Ol a5[a] MI 1	Ol n6 MI 1	Ol n16 MI 1	Ol a5 Rim Glass	Ol n6 Rim Glass	Ol n13 Rim Glass	Ol-02-1 MI 1	Ol 11 Mean	Ol n30 Mean	Ol n8a,b Mean
N[c]	20	3	3	5	5	2	3	7	3	5	5	5	3	14	12	5
SiO_2	48.24	47.34	48.79	50.04	50.71	49.56	48.15	47.97	48.88	50.99	51.78	50.77	48.64	47.97	47.74	47.70
TiO_2	0.97	1.02	0.87	0.89	0.91	1.03	0.96	0.89	0.90	0.94	1.06	0.93	0.98	0.86	0.91	0.87
Al_2O_3	15.43	14.68	17.55	18.29	17.80	16.40	15.74	15.53	15.89	18.05	17.29	17.65	16.03	16.15	15.76	15.82
FeO_{tot}	6.97	8.75	7.33	7.88	7.91	5.93	5.94	5.75	5.76	7.47	8.16	7.76	7.18	7.57	6.43	6.14
MnO	0.13	0.26	0.24	0.19	0.15	0.11	0.12	0.14	0.11	0.16	0.14	0.17	0.18	0.15	0.13	0.15
MgO	4.28	3.98	4.41	5.54	5.61	2.84	4.23	5.69	4.59	5.37	5.34	5.59	2.74	5.99	4.36	5.25
CaO	15.19	14.93	11.87	10.75	10.61	15.19	14.58	14.08	14.46	10.97	10.18	10.72	14.94	12.56	15.23	14.60
Na_2O	2.46	2.39	2.71	3.03	2.93	2.63	2.28	2.35	2.22	2.83	3.08	2.94	2.48	2.31	2.42	2.43
K_2O	1.71	1.67	1.93	2.29	2.36	1.48	1.43	1.31	1.36	2.11	2.74	2.27	1.74	1.63	1.71	1.76
P_2O_5	0.59	0.83	0.55	0.53	0.58	0.72	0.57	0.53	0.56	0.56	0.75	0.62	0.59	0.56	0.57	0.55
S	0.255	0.247	0.177	0.037	0.032	0.183	0.159	0.147	0.128	0.047	0.020	0.020	0.225	0.167	0.239	0.213
Cl	0.215	0.237	0.184	0.133	0.126	0.204	0.190	0.179	0.193	0.152	0.139	0.144	0.231	0.174	0.216	0.198
Total	96.43	96.32	96.61	99.61	99.74	96.27	94.34	94.57	95.04	99.64	100.68	99.57	95.96	96.10	95.72	95.66
CaO/Al_2O_3	0.98	1.02	0.68	0.59	0.60	0.93	0.93	0.91	0.91	0.61	0.59	0.61	0.93	0.78	0.97	0.92
K_2O/Na_2O	0.70	0.70	0.71	0.76	0.81	0.56	0.63	0.56	0.61	0.75	0.89	0.77	0.70	0.70	0.71	0.73
S/Cl	1.18	1.04	0.96	0.28	0.26	0.89	0.83	0.82	0.66	0.31	0.14	0.14	0.97	0.96	1.11	1.07
Olivine[d]																
Fo	88.4	85.0	86.5	86.0	84.7	89.3	88.7	89.5	89.6	86.8	85.9	85.8	88.2	87.5	88.0	89.3
SiO_2	40.79	39.86	40.40	40.07	39.96	40.92	40.27	40.07	40.95	40.79	40.14	39.97	41.04	40.26	40.41	40.47
MgO	47.48	45.07	46.18	46.11	44.82	48.28	48.00	48.21	47.86	46.21	45.82	45.92	47.72	47.01	47.42	47.79
FeO	11.06	14.13	12.82	13.39	14.45	10.33	10.85	10.09	9.93	12.51	13.45	13.58	11.35	11.93	11.49	10.19
MnO	0.24	0.37	0.18	0.05	0.29	0.00	0.22	0.21	0.17	0.19	0.18	0.20	0.28	0.41	0.12	0.27
CaO	0.45	0.57	0.41	0.39	0.47	0.47	0.26	0.26	0.26	0.30	0.41	0.33	0.29	0.38	0.35	0.29
						Recalculated Compositions[e]										
SiO_2	47.66	46.76	48.33			48.70	47.74	47.81	48.46				47.77	47.73	47.31	47.33
TiO_2	0.89	0.94	0.83			0.93	0.91	0.87	0.85				0.87	0.83	0.86	0.83
Al_2O_3	14.23	13.55	16.60			14.77	14.92	15.22	15.07				14.19	15.64	14.84	15.03
FeO_{tot}	7.28	9.17	7.63			6.36	6.19	5.83	5.98				7.66	7.71	6.73	6.34
MnO	0.12	0.24	0.23			0.10	0.11	0.14	0.10				0.16	0.14	0.12	0.14
MgO	7.64	7.14	6.67			7.34	6.51	6.54	6.84				7.91	7.30	6.89	7.37
CaO	14.05	13.82	11.25			13.73	13.84	13.81	13.72				13.26	12.18	14.36	13.88
Na_2O	2.27	2.20	2.57			2.37	2.16	2.30	2.11				2.19	2.24	2.28	2.30
K_2O	1.58	1.54	1.82			1.34	1.36	1.28	1.28				1.54	1.58	1.61	1.67
P_2O_5	0.54	0.77	0.52			0.65	0.54	0.52	0.53				0.52	0.54	0.54	0.52
S	0.235	0.228	0.168			0.164	0.150	0.147	0.121				0.199	0.162	0.225	0.203
Cl	0.198	0.219	0.174			0.184	0.180	0.175	0.183				0.204	0.169	0.203	0.189
X_{Fo}[f]	0.08	0.08	0.05			0.10	0.05	0.02	0.05				0.12	0.03	0.06	0.05

[a]End-member compositions in MELTS calculations (see text).
[b]From *Métrich et al.* [2001].
[c]Number of analysis.
[d]Host olivine composition as [100 × Mg/(Mg + Fe)]. In mol %.
[e]Composition recalculated on the basis of $K_D = [(FeO/MgO)_{ol}/(FeO/MgO)_{melt}] = 0.29$.
[f]Fraction of olivine crystallized after entrapment.

display a wide compositional range (Fo_{68}–Fo_{86}), but in each crystal the chemical contrast is highly variable. A careful observation of thin sections reveals that the MI trapped in either the Fe-rich zones or the mottled areas of the reverse-zoned crystals are brownish, isolated with a rounded ovoid shape and size between 30 μm and 100 μm (Figure 1g). Although they look like typical primary inclusions with regular rounded shapes and one bubble, they are related to dissolution-crystallization processes as discussed further. They are easily distinguished from the clear and elongated melt inclusions actually trapped during crystal growth (Figure 1h).

5. Chemistry of Melt Inclusions and Rim Glasses

5.1. Major Elements

[15] The representative compositions of MI and rim (matrix) glasses (glass fragments adhering to the crystals) in the ST81 and ST 207 pumice samples are reported in Table 2. Since the discussion involves generalization of these new data in the context of published results on MI hosted in olivines from pumices (ST79 and ST82 samples [*Métrich et al.*, 2001]), some of the previous data are also presented in Table 2. The entire previous data set is available on the Web site www.petrology.oupjournals.org.

[16] The MI compositions were corrected for postentrapment crystallization by adding olivine component whose composition is determined in the vicinity of the inclusion, in order to get olivine-liquid equilibrium with K_D $[(FeO/MgO)_{ol}/(FeO/MgO)_{melt}] = 0.29$ for Stromboli melts, and $[Fe^{3+}/(Fe^{2+} + Fe^{3+})] = 0.2$. The effect of postentrapment crystallization of olivine on most MI compositions is limited and should not significantly affect the ratio between elements, except for Fe and Mg, the volatile concentrations and the assessed fluid pressures (PCO_2, PH_2O). In the discussion, only the major element and volatile concentra-

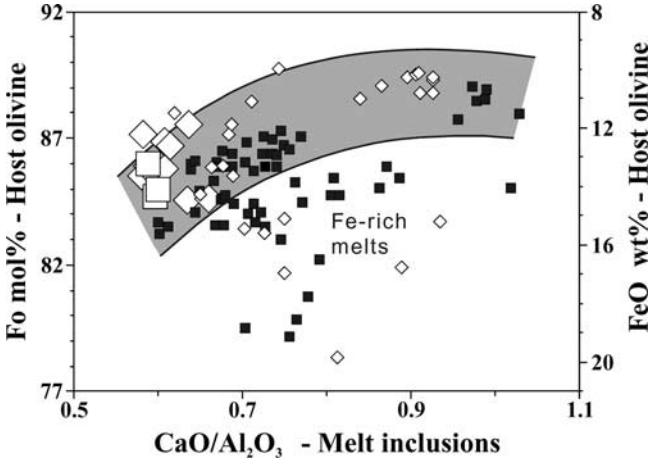

Figure 2. CaO/Al_2O_3 ratio of melt inclusions versus Fo [100Mg/(Mg + Fe)] and FeO content of host olivine. Composition of rim glasses adhering to the crystal faces plotted against the Fo content of the olivine outer rim. The shaded area shows the general evolutionary trend delineated on the basis of the clear MI in homogeneous olivine. Solid square, St81 melt inclusions; open diamond, St207 melt inclusions; large open symbols, rim glasses.

tions corrected for postentrapment olivine crystallization, have been considered.

[17] MI and rim glasses display a wide range of compositions (CaO/Al_2O_3 = 1–0.59; K_2O/Na_2O = 0.56–0.89; K_2O = 1.28–2.74 wt %). The most primitive compositions are by far less evolved than those of the whole rocks (CaO/Al_2O_3 = 0.65 and 0.63 in St81 and St207, respectively).

[18] The MI with clear color and elongated morphology together with rim glasses depict a general evolutionary trend with CaO/Al_2O_3 ratio decreasing from ~1 in Fo_{89-90} to 0.59–065 in Fo_{83-87} (Figure 2). Conversely, the brownish, rounded MI trapped in crystals with reverse zoning, Fe-rich cores and relict patchy zones plot out of this trend. They have inconsistent CaO/Al_2O_3 ratios with respect to composition of their host olivines which were analyzed in the vicinity of the inclusions. The distinction between the two main populations of crystals and MI is illustrated in a binary diagram $FeO_{olivine}$ versus FeO_{MI} (Figure 3). It is well known that MI, particularly in magnesian olivine, may have experienced partial even total reequilibration after entrapment, mainly depending on the temperature gradient during cooling [*Danyushevsky et al.*, 2000, 2002]. This process results in MI depleted in FeO with respect to the originally trapped melt and cannot be totally excluded in the case of some MI in the most magnesian olivines of the St207 sample (Table 2). However, the clear MI hosted in homogeneous olivines, including the most primitive Fo_{88-89} together with the whole rock and matrix glasses define a same trend of olivine-liquid equilibrium as exemplified in St81 sample (Figure 3).

[19] In summary, we have considered that the clear MI in homogeneous olivines, both in samples St207 and St81, are closely representative of the magmatic system with respect to their major elements. MI in reverse-zoned crystals have higher FeO_{total} content that can reach 12 wt %. Although they may be in equilibrium in a system olivine-liquid, with respect to their FeO/MgO ratio because of possible reequilibration, they have been considered neither as representative of the whole melt nor in equilibrium with the carrier magma. Particularly, the high FeO content in melt and their Fe-rich host would indicate rather evolved terms but disagrees with high CaO content and CaO/Al_2O_3 ratio. The FeO-rich MI recorded open system processes that changed their initial composition as will discuss further. These MI will be referred as MI in disequilibrium conditions.

5.2. Trace Elements

[20] Trace elements were determined by SIMS in nine melt inclusions including MI that have recorded disequilibrium conditions. The REE patterns indicate enrichment in LREE with La/Dy ratio ranging from 7.5 to 10.4 without significant difference between the two populations (Table 3 and Figures 4a and 4b). However, the most primitive MI display high Cr concentration (up to 210 ppm) and CaO/Al_2O_3 ratio (~1), but have intermediate La/Yb ratio ~9 and the highest La and Ce contents that is inconsistent with a simple crystal fractionation process (Figures 4c and 4d).

5.3. Volatile Constituents

[21] The melt inclusions show a wide range of volatile concentrations with up to 2450 ppm S, 2000 ppm Cl in olivine Fo_{88-89} (ST81) and 1520 ppm S, 1915 ppm Cl in Fo_{90} (ST207). In both samples, S and Cl decrease in MI and embayments as the melt compositions progressively evolve. The lowest contents are measured in rim glasses which still contain 430–200 ppm S and 1520–1390 ppm Cl. The rather high sulfur content in rim glasses indicate a rapid decompression and quench without time for total equilibrium at one atmosphere at which S concentrations should be <70 ppm [*Métrich et al.*, 2001]. As a result the S/Cl ratio decreases from 1.2 to 0.26 in ST81 pumice and from ~0.8 to 0.14 in ST207 pumice (Table 2).

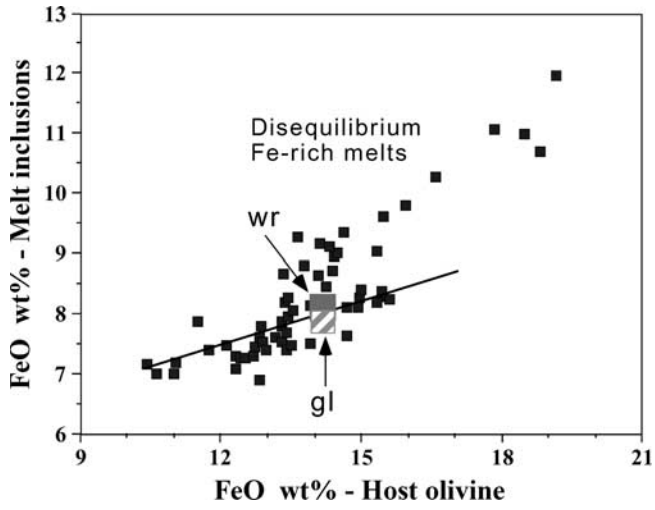

Figure 3. FeO content of melt inclusions as a function of FeO content of host olivine in St81 sample. The line groups clear elongated melt inclusions hosted in homogeneous crystals, whole rock (wr) and rim glass (gl). The anomalous high Fe content is measured in brownish melt inclusions in disequilibrium conditions.

Table 3. Major and Trace Element, S, and Cl Concentrations in Selected Melt Inclusions of St81 Pumice Sample

	Ol 11 MI1	Ol n10 MI3	Ol n56 MI1	Ol14 MI1	Ol13 MI2	Ol13 MI3[a]	Oln51 MI1	Oln55 MI2[a]	Oln9 MI2[a]
N[b]	3	3	2	3	3	2	3	3	2
SiO_2	47.97	48.49	49.13	49.35	49.32	48.18	47.75	47.77	47.65
TiO_2	0.96	0.89	0.91	0.92	0.92	0.82	1.00	0.98	0.98
Al_2O_3	14.62	16.52	17.06	17.08	16.62	15.63	13.88	16.28	15.63
FeO_{tot}	7.62	7.12	6.83	7.63	7.84	8.34	9.16	8.96	11.37
MnO	0.13	0.10	0.14	0.18	0.23	0.25	0.26	0.16	0.29
MgO	5.06	3.97	3.06	4.74	4.95	4.60	5.54	4.63	3.33
CaO	15.02	12.49	13.12	11.43	11.85	13.61	14.15	13.15	11.81
Na_2O	2.39	2.50	2.71	2.67	2.58	2.50	2.27	2.28	2.33
K_2O	1.67	1.94	2.15	2.08	1.99	1.76	1.49	1.32	1.66
P_2O_5	0.57	0.53	0.58	0.55	0.56	0.57	0.57	0.56	0.52
S	0.251	0.210	0.232	0.180	0.185	0.228	0.262	0.219	0.185
Cl	0.217	0.188	0.202	0.182	0.177	0.196	0.226	0.182	0.189
Total	96.48	94.97	96.12	96.98	97.22	96.70	96.55	96.50	95.93
CaO/Al_2O_3	1.03	0.76	0.77	0.67	0.71	0.87	1.02	0.81	0.76
S/Cl	1.16	1.12	1.15	0.99	1.05	1.16	1.16	1.20	0.98
Fo[c]	88.0	86.6	87.0	86.0	85.7	85.9	85.2	85.4	79.2
				Recalculated Compositions[d]					
SiO_2	47.48	48.00	48.40	48.93	48.95	47.69	47.41	47.27	47.00
TiO_2	0.90	0.83	0.83	0.88	0.88	0.77	0.96	0.91	0.90
Al_2O_3	13.65	15.50	15.61	16.31	15.96	14.63	13.25	15.14	14.42
FeO_{tot}	7.88	7.47	7.30	7.88	8.07	8.66	9.38	9.29	11.97
MnO	0.13	0.10	0.13	0.17	0.22	0.23	0.24	0.15	0.26
MgO	7.84	6.58	6.75	6.59	6.58	7.22	7.32	7.46	6.22
CaO	14.06	11.74	12.04	10.93	11.40	12.77	13.53	12.26	10.93
Na_2O	2.23	2.35	2.48	2.55	2.48	2.34	2.16	2.12	2.15
K_2O	1.56	1.82	1.97	1.98	1.91	1.65	1.42	1.23	1.53
P_2O_5	0.53	0.50	0.53	0.53	0.54	0.54	0.55	0.52	0.48
S	0.234	0.197	0.212	0.172	0.178	0.213	0.250	0.203	0.171
Cl	0.202	0.176	0.185	0.174	0.170	0.183	0.216	0.169	0.174
X_{Fo}[e]	0.07	0.06	0.09	0.05	0.04	0.06	0.05	0.07	0.08
Sc	49	36	31	31	29	34	50	42	39
V	346	307	339	289	308	292	355	333	350
Cr	210	85	100	70	70	75	150	60	40
Rb	42	51	70	53	65	50	38	34	41
Sr	847	808	882	741	814	764	840	746	732
Y	30	26	30	25	28	26	31	27	30
Zr	141	142	164	136	151	140	139	114	143
Nb	23	21	26	21	24	20	22	16	20
Cs	3.8	4.5	4.9	7.6	4.9	4.5	4.0	2.8	4.6
Ba	936	974	1145	905	1051	920	906	724	807
La	61.1	54.6	61.3	47.9	56.6	52.5	63.5	44.5	51.5
Ce	116.1	103.0	122.2	92.2	111.0	98.8	123.1	86.8	98.0
Nd	55.3	48.8	55.0	48.4	50.9	47.9	60.3	42.9	47.6
Sm	11.5	10.4	10.2	9.2	9.0	9.7	11.8	9.4	11.4
Eu	3.1	2.87	2.49	2.63	2.29	2.46	2.98	2.53	3.1
Gd	8.8	8.1	8.3	7.2	8.2	7.4	10.0	8.5	7.9
Dy	6.8	6.2	5.9	5.7	5.6	5.7	7.2	5.9	6.7
Er	3.7	3.3	3.3	3.1	2.9	3.1	3.9	3.2	3.6
Yb	3.4	3.1	2.95	2.9	2.85	2.9	3.7	3.0	3.4
La/Yb	17.8	17.6	20.8	16.6	19.9	18.4	17.4	15.0	15.2

[a]FeO-rich melt inclusions.
[b]Number of analysis.
[c]Host olivine composition as [100 × Mg/(Mg + Fe)]. In mol %.
[d]Composition recalculated on the basis of $K_D = [(FeO/MgO)_{ol}/(FeO/MgO)_{melt}] = 0.29$.
[e]Fraction of olivine crystallized after entrapment.

[22] The carbon and water contents have also been measured in MI hosted in ST81 olivine (Fo_{79-87}) from the two populations. In every case, the results indicate high volatile content from 3.4 to 1.8 wt % H_2O, and from 1887 to 707 ppm CO_2 (Table 4). There is no clear relationship between the pressures deduced from dissolved volatiles and the composition of either the melts or the olivine crystals. Several inclusions were analyzed in one single grain and reveal a significant variation in both H_2O and CO_2. For example in one crystal Fo_{84} (oln7, Table 4), the H_2O concentration varies from 3.4 to 1.8 wt % and CO_2 from 1582 to 1017 ppm. According to *Papale*'s [1999] model, the pressures deduced from water and carbon dissolved in melts assuming equilibrium saturation vary from 4 to 2.9 kbar as a whole and form a cluster close to 3.5 kbar (Figure 5). These results are comparable with the few data previously obtained [*Métrich et al.*, 2001]. Isobars were also calculated using the program developed by *Newman and Lowenstern* [2002], for melts containing 49 wt % SiO_2 at 1140°C. Compared to *Papale*'s [1999] model, there is a shift toward lower values and the difference is nearly 500 bars at 3 kbar

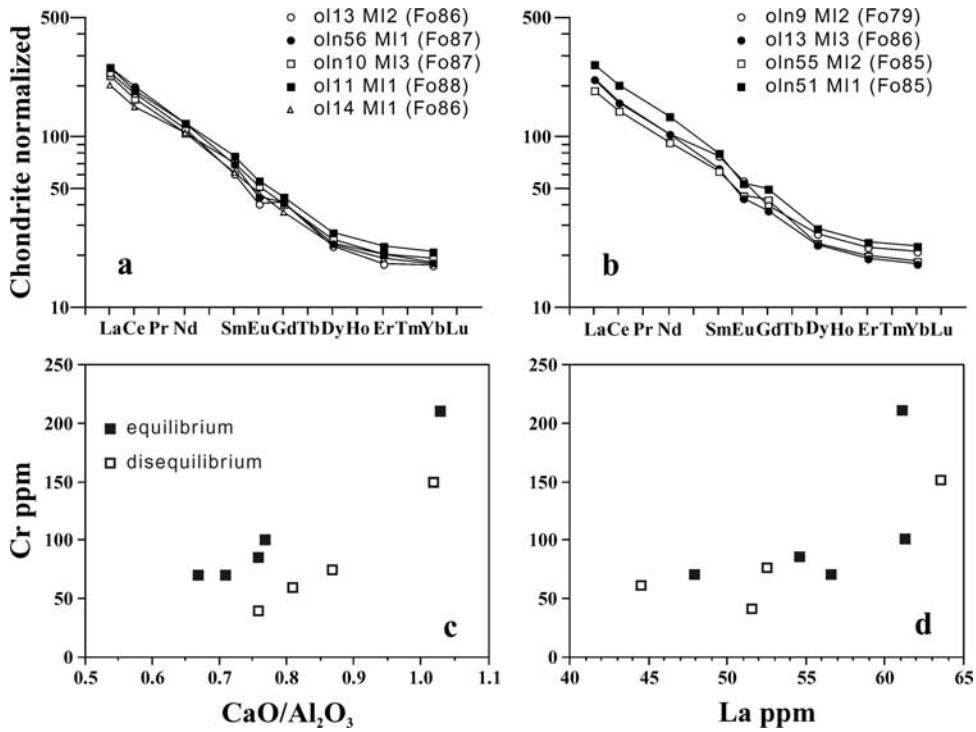

Figure 4. Chondrite-normalized REE patterns [*McDonough and Sun*, 1995] for melt inclusions of St81 sample, regarded as representative of the magma from which the olivine (a) grew (equilibrium) or (b) not (disequilibrium). Plots of (c) Cr content and (d) La content in the same melt inclusions versus CaO/Al_2O_3 ratio.

Table 4. Water and Carbon Concentrations in Melt Inclusions of Olivines

Sample	Fo,[a] mol %	K_2O,[b] wt %	S,[b] wt %	Cl,[b] wt %	CaO/Al_2O_3	H_2O, wt %	CO_2, ppm	H_2O Corr,[b] wt %	CO_2 Corr,[b] ppm
					St81				
Oln12-MI2	84.4	1.79	nd	nd	0.69	1.96	nd	1.84	nd
Oln12-MI1	84.4	1.79	0.169	0.171	0.71	2.16	850	2.03	799
Oln9-MI1	79.5	1.71	0.142	0.174	0.70	3.17	1195	3.04	1147
Oln9-MI3	79.9	1.83	0.148	0.193	0.76	2.85	nd	2.68	
Oln9-MI2	79.2	1.53	0.171	0.174	0.76	3.10	954	2.85	878
Oln9-MI4	81.8	1.53	0.170	0.176	0.68	2.96	nd	2.96	
Oln8-MI1	86.1	1.83	0.165	0.167	0.64	2.89	1181	2.69	1098
Oln8-MI2	86.3	1.92	0.166	0.170	0.69	2.23	2029	2.07	1887
Oln7-MI1	84.1	1.99	0.155	0.166	0.64	3.50	1266	3.36	1215
Oln7-MI2	84.0	1.80	0.165	0.175	0.71	3.45	1665	3.28	1582
Oln7-MI3	83.6	1.94	0.148	0.166	0.68	3.10	1385	2.95	1316
Oln7-MI4	83.6	1.99	0.194	0.194	0.67	2.67	1164	2.54	1106
Oln7-MI5	84.1	1.84	0.159	0.174	0.72	2.96	1071	2.81	1017
Oln10-MI2	86.7	1.78	0.180	0.175	0.75	2.52	852	2.34	792
Oln10-MI3	86.6	1.82	0.197	0.176	0.76	2.82	1281	2.65	1204
Oln10-MI1	86.9	1.84	0.183	0.171	0.73	2.76	1078	2.57	1003
Oln10-MI7	87.1	1.94	0.174	0.176	0.73	2.77	819	2.58	762
Oln10-MI6	85.9	1.86	0.170	0.172	0.70	2.73	1084	2.54	1008
Oln10-MI4	86.6	nd	nd	nd	nd	2.66	1067	2.50	1003
Oln10-MI5	86.6	nd	nd	nd	nd	2.30	752	2.16	707
Oln14-MI1	83.5	2.05	0.148	0.168	0.61	3.28	1152	3.18	1117
Oln14-MI2	83.2	2.10	0.152	0.173	0.60	2.81	885	2.75	867
Oln14-MI3	83.7	2.07	0.142	0.170	0.60	2.54	754	2.41	716
					St79p[c]				
Oln 30	88.0	1.61	0.225	0.203	0.97	2.40	1177	2.3	1107

[a]Fo is the host olivine composition as [100 × Mg/(Mg + Fe)].
[b]Concentrations corrected for the postentrapment crystallization of olivine; nd, not discernable.
[c]From *Métrich et al.* [2001].

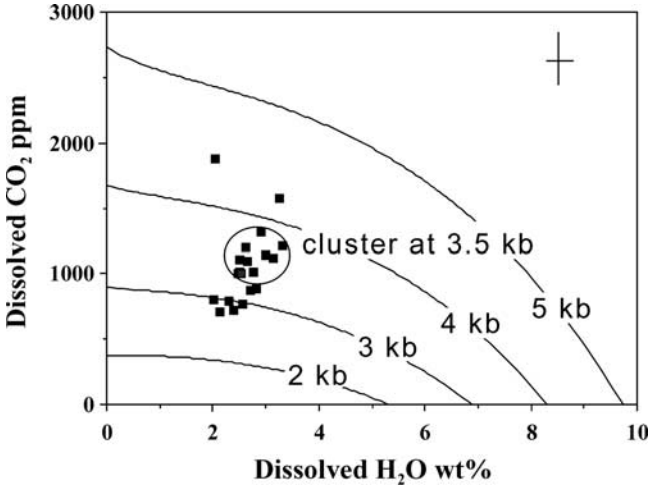

Figure 5. H_2O versus CO_2 contents measured in melt inclusions hosted in olivines (Fo_{79-87}) of St 81 sample. Isobaric curves according to *Papale* [1999].

considering a melt with 2.7 wt % H_2O and 0.11 wt % CO_2. Thus the total pressures calculated must be considered with caution because the CO_2 solubility in HK-basaltic shoshonitic melts rich in H_2O is still poorly experimentally constrained. However, the interval of variation (~1 kbar) is comparable between the two models.

6. Discussion

6.1. Significance and Interpretation of FeO-Rich Melt Inclusions

[23] We have examined the different processes able to explain the FeO-rich MI which also display high CaO/Al_2O_3 ratio and volatile concentrations. Some of them are similar (except for FeO) to MI in equilibrium with Fo_{89} (e.g., St81 Ol1 versus ol11 in Table 2; ol11 versus oln51 in Table 3). It has been suggested that oxidation of MI, related to hydrogen loss during heating experiments and its subsequent reequilibration with its host containing Fe^{2+} could result in some abnormal high total FeO content of the melt [see *Danyushevsky et al.*, 2002]. It is also thought that postentrapment H_2O loss and melt oxidation occur during one atmosphere heating stage experiments [*Danyushevsky et al.*, 2002; *Massare et al.*, 2002] or in cumulative bodies [*Massare et al.*, 2002] when the olivine and their MI were extracted and isolated from their parental melts. Such a process involving oxidation and partial reequilibration between MI and olivine cannot be totally excluded, however with a very limited effect, since the amount of dissolved H_2O is still high (up to 3.0 wt %; Table 4). The MI and mottled textures observed in these olivines suggest that they may have recorded dissolution and crystallization events, successively. Partial dissolution of olivine may create a network of channels either connected with the surrounding melt or isolated by recrystallization of the crystal to form melt inclusions. Experiments on olivine dissolution in silicate melts indicate that the dissolution is usually controlled by diffusion and that major element concentrations show anomalous diffusion profiles, with enrichment in Ca, Fe and depletion in Al, K at the interface reaction [uphill diffusion according to *Zhang et al.*, 1989]. Such diffusion profiles may explain the particularly low K_2O content down to 1.3 wt % associated with $CaO/Al_2O_3 \geq 1$ measured in some of these inclusions. However, the general tendency is marked by a chemical evolution toward the composition of the melt in which the olivine dissolved. The higher are volatile concentrations and the CaO/Al_2O_3 and S/Cl ratios, the most primitive is the melt which entrains and reacts with the olivine. We propose that these FeO-rich MI result from successive processes including (1) ascent of primitive melt blobs differing by their degree of differentiation, (2) entrainment and dissolution of preexisting (Fe-richer) olivines, (3) crystallization, and (4) possible postentrapment reequilibration.

6.2. Compositional Variability and Differentiation of the Parental CaO-Rich Melts

[24] In this discussion, the FeO-rich inclusions were excluded. Only MI considered as representative of the magma from which the olivine grew are discussed in comparison to other samples from paroxysmal eruptions [*Métrich et al.*, 2001]. In each of the analyzed paroxysmal events that occurred over the last 1400–1800 years, the olivines Fo_{88-91} with rather high NiO (0.16 to 0.22 wt %) and CaO (0.25 to 0.30 wt %) contents are rare but systematically present. The NiO and CaO contents, respectively lower and higher than the contents of typical mantle olivines [*Sato*, 1977; *Gurenko et al.*, 1996] indicate that the Mg-rich olivines do not represent products of disaggregation of mantle xenoliths but crystals of mantle-derived magmas which suffered limited fractional crystallization. In St207 pumice, the Cr-spinel-olivine pair falls close to the olivine-spinel mantle array defined by *Arai* [1987] and attests to the primitive nature of the crystals.

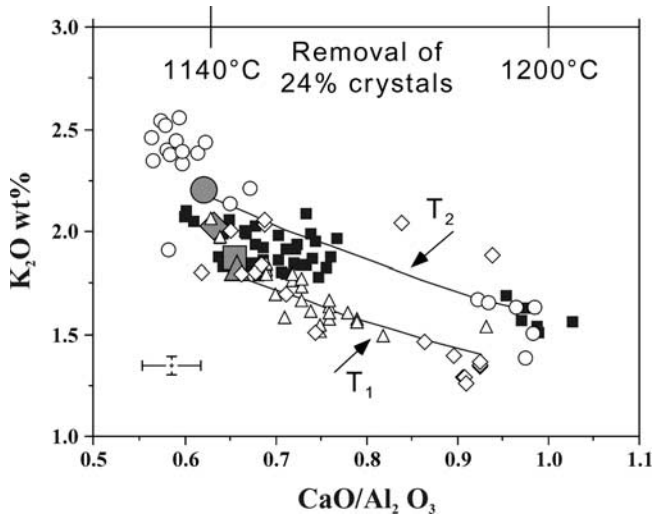

Figure 6. CaO/Al_2O_3 ratio versus K_2O of melt inclusions (except FeO-rich MI). T1 and T2, crystallization paths calculated by using MELTS code [*Ghiorso and Sack*, 1995] (see text for explanation). Solid square, St81 melt inclusions; open diamond, St207 melt inclusions; open triangle, St82 melt inclusions; open circle, St79 melt inclusions (data from *Métrich et al.* [2001]); gray symbols, whole rock composition.

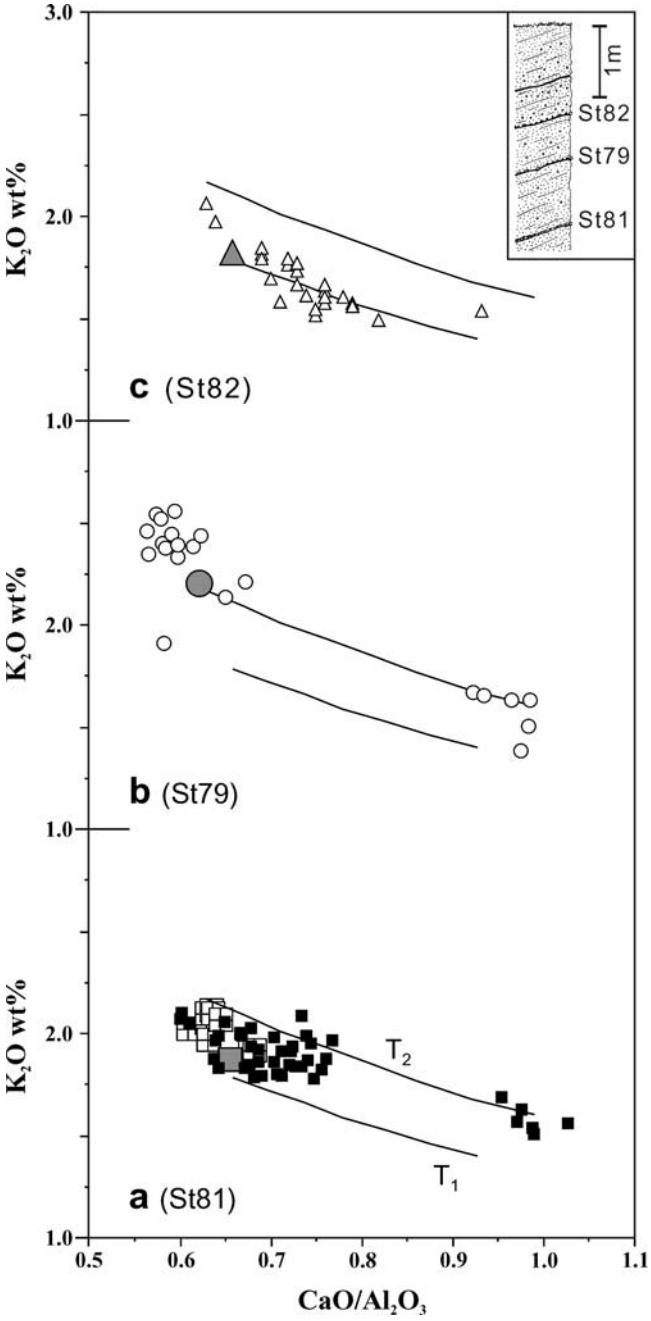

Figure 7. Variations of CaO/Al_2O_3 ratio versus K_2O of melt inclusions in equilibrium with their host olivine along a stratigraphic trench (trench 2 of *Rosi et al.* [2000] and *Métrich et al.* [2001]). Inset shows the stratigraphic section. Crosses, embayments; T1, T2, and other symbols are as in Figure 6.

[25] In every case, the MI in primitive olivine display CaO/Al_2O_3 ratio > 0.9 (Figure 6), high concentrations in CaO (up to 14.5 wt %) and low content in FeO (6–7 wt %). We consider this low FeO content as a real fingerprint of the parental magmas, since the whole rocks have similar characteristics. Therefore these inclusions are regarded as representative of the CaO-rich, Fe-poor parental melts that feed the current activity at Stromboli. Comparable CaO-rich arc-derived melts with rather low FeO content and MgO/FeO ratio close to 1 have been rarely described. They are reported at Vulcano (Aeolian islands, Italy), Grenada (Lesser Antilles) and Nicaragua (Central America) as reviewed by *Schiano et al.* [2000]. These CaO-rich, SiO_2 undersaturated primary arc melts would imply the involvement of clinopyroxenite during melting source process, either as clinopyroxenite cumulates under upper mantle conditions [*Schiano et al.*, 2000] or veined mantle [*Kamenetsky et al.*, 1995]. However, the question regarding the origin of Ca-rich melts at Stromboli needs specific geochemical studies to be addressed.

[26] At Stromboli, the CaO-rich melts have fairly variable K_2O content between 1.9 to 1.3 wt % (Table 2 and Figure 6). In order to discuss the relationship between these CaO-rich primitive melts and the magmas erupted as HK-basaltic pumices, we tested the extent of the crystal fractionation by using MELTS code [*Ghiorso and Sack*, 1995]. We have considered two end-members representative of parental melts with 1.6 and 1.35 wt % K_2O and $CaO/Al_2O_3 \sim 1$. (Table 2 and Figure 6). Their liquidus temperature is 1205–1195°C for 2.5 wt % water at 4 and 3 kbar, respectively. On the basis of the calculated crystallization paths, the composition of whole rocks ($CaO/Al_2O_3 = 0.63–0.65$) is obtained from parental melts by crystallizing 24 wt % solid, mainly clinopyroxene, with a temperature decrease of about 60°C (Figure 6). The two trends calculated from the two melt end-members, labeled as T1 (lowest K_2O content) and T2 (highest K_2O content) in Figure 6, delineate a domain that encompasses the whole chemical variation of both the whole rocks and MI. They also indicate that crystal fractionation only from one single parental magma cannot reproduce the compositional variability in one single sample (e.g., St81 and St207, Figure 6).

[27] By considering samples in chronological order from the base to the top of the stratigraphic trench (Figure 7), pumice St81 from the lowest tephra layer (Figure 7a) cannot be derived from K_2O-richest melts (T2) recorded as inclusions in the most primitive olivine present in the same sample. Assuming a crystal fractionation process, the suitable parental magma at the origin of this pumice is intermediate between the two end-members. Similarly, most inclusions do not follow a simple fractionation trend as supported by the fact that the less evolved MI with high Cr content also display the highest La and Ce concentrations and intermediate La/Yb ratio (Figure 4). All together, the inclusions define a mixing trend between magmas that differ by both their degree of differentiation and K_2O content. However, mixing is only recorded on the micrometer scale by inclusions and their hosts since the whole rock does not evidence significant chemical heterogeneity except in its mineralogy. As a result, the K_2O-rich primitive magma that entered the deep system did not evolve and did not erupt. It had not significantly influenced the composition of the pumice produced during the eruption.

[28] Conversely, this K-rich parental melt produced the pumice St79 erupted during the following paroxysmal eruption, whereas parental melt with the lowest K_2O content was present only as inclusions in olivine Fo_{89} (Figure 7b). Finally the pumice ST82 from the youngest tephra layer clearly illustrates crystal fractionation from primitive melts, with the lowest K_2O content, akin to those trapped in magnesian olivine in the precedent eruption

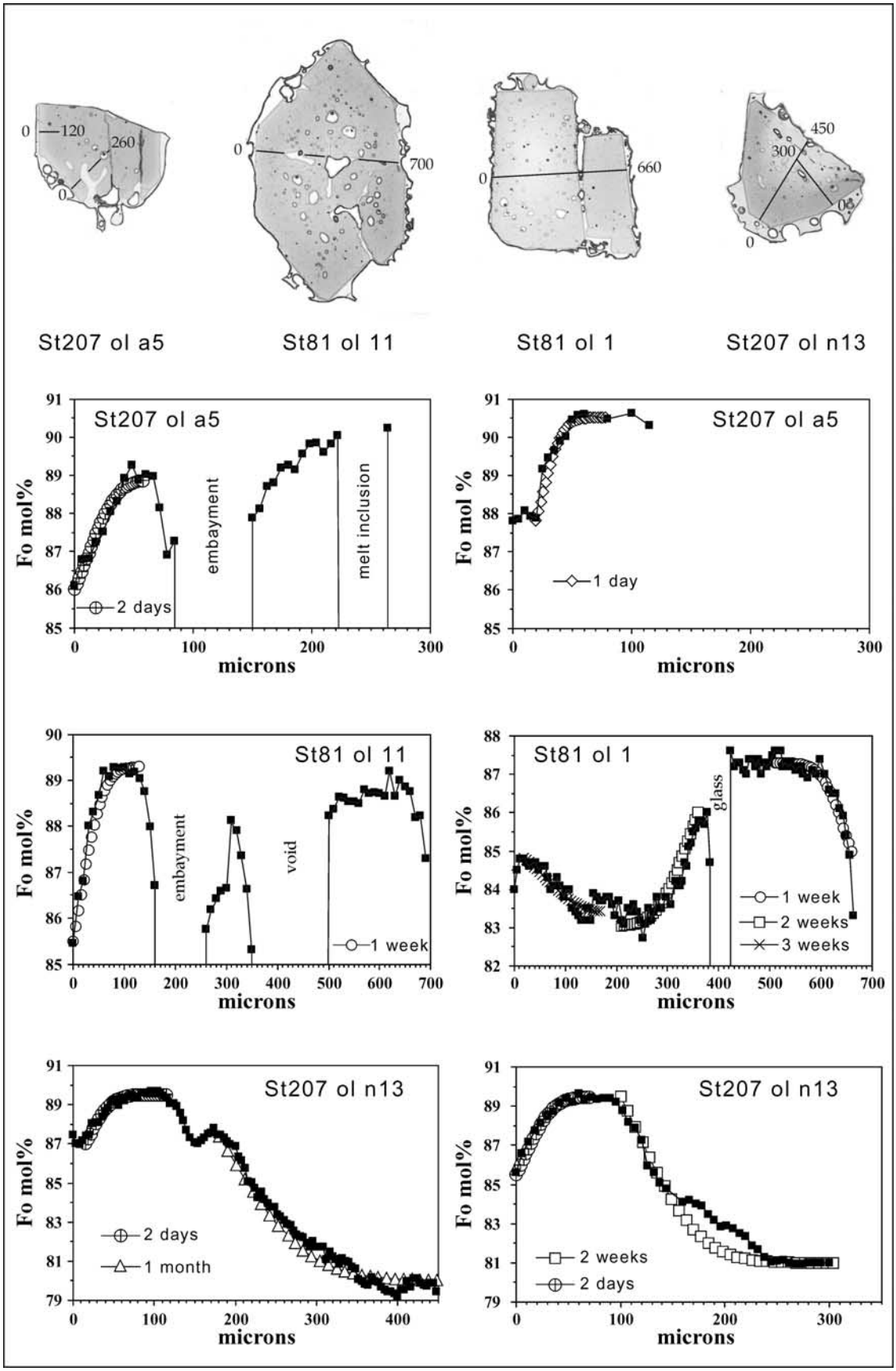

Figure 8. Compositional traverses (solid square) measured in representative olivines and calculated diffusion profiles (the diffusion times are indicated). Sketches of selected olivines and direction of compositional traverses are shown.

(Figure 7c). The pumice erupted during the major explosions in August 1998 and 1999 belong to the same trend (Table 1).

[29] In any case the composition of the pumice erupted during paroxysmal eruptions testifies to the recurrent variability of the parental magmas between two end-members distinct by their K_2O content and most likely trace element (e.g., La, Ce). From the stratigraphic record the chemical change in composition of both the most primitive melts that intruded the system and the basaltic magmas erupted at the surface seems to define a bimodal system. However, intermediate compositions exist as illustrated by the St207 sample (Figure 6) and pumices collected from other stratigraphic trenches [*Rosi et al.*, 2000].

[30] Since the Ca-rich melts which ascent do not clearly affect the bulk composition of the pumice, the volume of new magma batch is most likely several orders of magnitude smaller than that of the basaltic magma that produces the pumice.

6.3. Implications for the Deep Feeding System

[31] All MI, including the FeO-rich MI, have recorded high total fluid pressure regardless of their extent of crystallization (CaO/Al_2O_3 = 0.76–0.60) and the composition of their host (from Fo_{87} to Fo_{79}). Assuming equilibrium saturation, the overall variation of the inferred pressures suggests that entrapment proceeded within 1 kbar range of pressure (Figure 5). There is no clear relationship between the pressures deduced from dissolved volatiles and the composition of either the melts or the olivine crystals. The high density of irregular MI and embayments observed in olivines Fo_{87-83} and the variable ratio between melt and gas bubble support the hypothesis of entrapment of gas oversaturated melts during decompression, dynamic magma mixing and crystallization. We cannot exclude that overpressure may have been caused by the uprising of primitive volatile-rich melts. In this hypothesis, the total fluid pressure assessed could be overestimated. However, similar pressures (~3–3.5 kbar depending on the model used for pressure calculations) have also been recorded in MI, hosted in Fo_{87-88}, representative, primitive melt blobs (Table 4).

[32] All these observations strongly suggest a turbulent regime where primitive volatile-rich melt blobs ascend in a vertically elongated conduit, mix with melts slightly different by their degree of evolution, exsolve gaseous constituents and crystallize. During ascent, the melt blobs reentrain and react with preexisting crystals to form the mottled olivines and the FeO-rich MI.

[33] All the features recorded by the MI and their host (composition, morphology and vapor saturation) implying dynamic processes were preserved in magma blobs expelled during the most violent explosions at Stromboli and provide an almost instantaneous image of the deep system. They also suggest that magmas progress and differentiate in a dike-like system with crystal-wrapped marginal parts. The mineral paragenesis along the margins is most likely represented by olivine and Ca-pyroxene since the diopside is the main phase of the pumice mineral assemblage and is computed as liquidus phase (MELTS [*Ghiorso and Sack*, 1995]). Accordingly, this system would be chemically zoned (or heterogeneous) at depth. This chemical heterogeneity seems to be mainly recorded in MI and difficult to assess in the bulk rocks at least on the basis of major element chemistry.

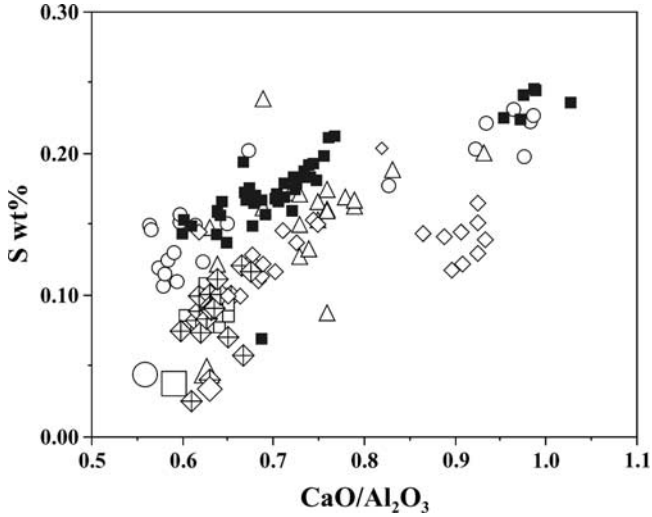

Figure 9. CaO/Al_2O_3 ratio versus S content of melt inclusions (except FeO-rich MI). The trend of sulfur degassing is particularly well illustrated in MI from samples St81 and St79, since their chemical evolution is mainly controlled by crystal fractionation whereas the effects of mixing are limited. Large open symbols, average rim glasses; crosses, embayments; other symbols are as in Figure 6.

6.4. Timescale Constraints on Mixing and Nucleation Processes

[34] The time interval between the arrival of Ca-rich primitive magmas in the deep feeding system and eruption was estimated on the basis of the extent of the reverse or normal zoning of crystals. Zoning profiles were measured on selected crystals chosen with backscattered electron analyses as representative of the different populations (Figure 8). We have interpreted all the zoning profiles in both normal and reverse zoned crystals, in terms of diffusive reequilibration between core and rim with either less or more evolved composition than Fo_{85-86}. The normal-zoned crystals have been considered as representative of mixing processes between Ca-rich primitive melts and the resident magmas. In this case, mixing induced the rapid growth of Mg-rich olivines as skeletal or composed crystals rimmed by olivine in equilibrium with the most evolved liquid. In the case of reverse-zoned crystals, evolved cores acted as nuclei and favored the crystallization of the primitive magma batches entering the crystal cumulate along the margins of the deep feeding system. Both processes may have been recorded in one single crystal, i.e., an early interaction between a primitive magma and an evolved olivine, followed by mixing between the primitive magma and the resident magma (olivine n13, St207 sample, Figure 1e).

[35] Diffusion profiles were calculated for different time intervals, following the formulation of *Carslaw and Jaeger* [1959] for the diffusion into a sphere. For the diffusion calculation we considered that the time for dissolution and growth was negligible and assumed the measured rim

composition as a fixed boundary condition. The interdiffusion coefficients applied are those determined by *Jurewicz and Watson* [1988]. The measured compositional profiles and the calculated profiles that best fit the data are reported in Figure 8. The times required for the development of the normal zoning profiles are short and fairly homogeneous ranging from 1 day to 1 week. In reverse-zoned olivines the diffusion profiles indicate a span of time between 1 week and 1 month. Variations in calculated time in one single crystal is attributed to asymmetric section of the crystal (Figure 8) and to some error due to the fact that diffusion profiles in evolved cores could be to some extent influenced by diffusional-homogenization processes between the crystal and the poorly evolved melts. Therefore they are not completely described by the diffusion equation into a homogeneous sphere.

[36] Finally, we have evaluated the span of time between the eruption and the nucleation of homogeneous olivines (Fo_{86-83}) in equilibrium with HK-basaltic melts, somewhat different by their degree of evolution. We used growth rate (G) calculated by *Donaldson* [1975] and *Jambon et al.* [1992], and assumed that G possibly remained constant during crystal growth as suggested by the homogeneous distribution of MI inside the crystals. Using the G values of *Donaldson* [1975] (2×10^{-7} cm s^{-1} to 6×10^{-7} cm s^{-1}), calculated for mild supercooling of 10°–30°C which are compatible with the olivine morphology, the time required for the growth of a 1000 μm olivine varies from 139 to 46 hours. *Jambon et al.* [1992] determined higher G values from 1.9×10^{-6} cm s^{-1} to 6.7×10^{-6} cm s^{-1}, for olivine growing from an anhydrous tholeiitic glass at 15°C and 30°C supercooling, respectively. The calculated times in the order of 14–4 hours are significantly shorter. They could even be lowered owing to the high water content of Stromboli melts. The high density of elongated and interconnected melt inclusions reflects a rapid growth of the olivine crystals and an equally rapid closure of skeletal embayments that possibly support high G.

[37] Because the olivine crystals are always smaller than 1000 μm the span of time between the crystal nucleation and the eruption should be in the order of 46–4 hours. In case of equilibrium saturation, this should be a maximum ascent time of the most primitive melts that trigger the paroxysmal events, during decompression from 3.5 kbar (fluid pressure).

6.5. Inferences on Sulfur Degassing

[38] The most primitive melts also differ by their S content and S/Cl ratio that range from nearly 0.23 to 0.15 wt % and 1.2 to 0.8, respectively (Table 2). The higher the K_2O content, the higher the S/Cl ratio. During magma crystallization and mixing, sulfur concentrations decrease (Figure 9). Sulfur degassing during crystal fractionation is illustrated in two of the pumices (St79 and St82). Their parental melts contain between 0.20 and 0.23 wt % S whereas the MI whose composition are closely similar to those of the whole rocks ($CaO/Al_2O_3 = 0.63–0.66$) contain no more than 0.17 to 0.15 wt % S. It implies that after 24% removal of crystals the melt possibly lost between 15 and 30% of the initial S content. Consequently significant quantity of S may be released during the first stage of differentiation and SO_2 gas emissions are partly sustained by the deep-seated magma which is crystallizing. These melts are not saturated with respect to a S-rich condensed phase since immiscible sulfide globules were never found and sulfur is mainly controlled by the vapor phase. Sulfur degassing has been discussed in relation to its strong partitioning in H_2O-rich vapor phase [*Carroll and Webster*, 1994; *Gerlach et al.*, 1996; *Scaillet et al.*, 1998; *Keppler*, 1999; *Wallace*, 2001]. This process explains the low-pressure release of sulfur at Stromboli [*Métrich et al.*, 2001]. However, the gas phase becomes richer in CO_2 as the pressure increases. For example, at 3 kbar, H_2O represents ~30 mol.% of a gas phase equilibrated with a basaltic magma containing 49 wt % SiO_2, 2.5 wt % H_2O and 1000 ppm CO_2 according to *Newman and Lowenstern* [2002]. Recent X-ray microspectroscopy experiments performed in similarly oxidized H_2O-rich MI from samples of Stromboli, rich in both CaO and H_2O show that sulfur is dissolved as sulfate (S^{VI}, SO_4^{2-}) and sulfite (S^{IV}, SO_3^{2-}) [*Métrich et al.*, 2002]. According to these authors, sulfite (S^{IV}) is highly reactive with silicate melts, and may explain the S release through the reaction $SO_{3\ melt} = SO_{2\ gas} + 1/2\ O_2$. Assuming sulfite solubility in the melts in the order of 250 ppm, the sulfite species must be renewed to sustain S degassing, through the reduction of sulfate following the reaction $SO_4 = SO_3 + 1/2\ O_2$. The sulfate breakdown requires a change in either the oxygen fugacity or the melt composition or both. Crystal fractionation dominated by the removal of Ca-rich pyroxene, significantly lowers the CaO content of the melt and possibly causes the reduction of the sulfate species. The crystal fractionation of CaO, H_2O-rich melts and their chemical evolution significantly affect the sulfur solubility. We propose that the sulfur partitioning in the gas phase starts during the early stage of crystallization and could be initiated at rather high pressure (possibly as high as 3–3.5 kbar).

7. Conclusions

[39] Since the beginning of the present activity, the buoyant uprise of deep-originated magma blobs has triggered paroxysmal explosions that suddenly interrupt the normal persistent activity. During paroxysms a maximum volume of $10^3–10^5$ m^3 of HK-basaltic pumice is erupted. The olivines and their melt inclusions preserved in the pumice of paroxysms have unraveled processes that have operated in the deep feeding system at Stromboli. We have been able to identify crystals growing during magma ascent. These crystals hold a particularly high density of irregular clear melt inclusions, often still connected each others, and gas bubbles. Conversely, preexisting crystals entrained by the ascending melt blobs developed rounded typical melt inclusions not representative of the carrier magma, but resulting from successive dissolution-crystallization processes.

[40] Each paroxysmal event evidences the arrival of primitive magma batches rich in CaO and poor in FeO. Their recognition is exceptional and only associated with the most energetic explosive events. They entered the deep feeding system possibly a few days before the eruption. The HK-basaltic magmas that sustain the present-day activity at Stromboli derive from the Ca-rich primitive melts by on average 24% crystallization within a range of temperature from 1205°–1195°C to 1135°–1145°C (MELTS [*Ghiorso*

and Sack, 1995]). All the MI analyzed for H_2O and CO_2 preserved total fluid pressures up to 3–3.5 kbar (PH_2O + PCO_2), assuming equilibrium vapor saturation. Assuming a flux rate of magma between 0.01 and 0.02 $km^3\ yr^{-1}$ [*Allard et al.*, 1994] the volume of the crystal mush, resulting from crystal fractionation, and has been built up along the walls of the most likely dike-like deep system over the last 1500 years, achieves 3.5–7 km^3. Crystal fractionation also induces a significant degassing of sulfur that may be at least 15%. We propose that SO_2 exsolution in the gas phase is controlled by the presence of sulfite dissolved in the melt and the reduction of sulfate in response to clinopyroxene crystallization and Ca lowering in melt.

[41] Crystal fractionation is the suitable mechanism to account for the HK-basaltic magmas which have erupted. However, there is also evidence for mixing events between melts slightly distinct in composition that strongly suggests that the feeding system is chemically zoned or heterogeneous at depth, at least at small scale. The timescale for mixing events and for reequilibration between melt inherited crystals, assessed from the diffusion profiles of olivines, although variable, may be as short as in the order of the week or the month. It infers turbulent convection in low viscosity basaltic melts and dynamic processes that are particularly well illustrated when the magma blobs are expelled as pumice. Size and shape of olivines, as well as the high density of irregular melt inclusions and melt/gas ratio in the inclusions, are consistent with rapid (from 46 to 4 hours, possibly less) crystallization of gas oversaturated magma during decompression. Moreover, the low crystal content and the absence of microlites indicate that the ascent occurred rapidly, such as to inhibit volatile-loss-induced crystal nucleation. This is also in good agreement with the absence of gas/liquid decoupling during magma ascent, i.e., that, at least in its final stage, the magma rose as a fast moving blob of low-density magmatic foam. Dynamic crystallization, mixing and gas exsolution and then buoyant ascent of small masses of magma appear to be not reported at other basaltic volcanoes as clearly as at Stromboli. We believe that this process could have a key role in sustaining the steady state activity at Stromboli which is lasting since 1400–1800 years.

[42] **Acknowledgments.** We thank A. Sobolev, L. Mastin, and an anonymous reviewer for their careful reviews; P. Allard, and M. Treuil for useful discussions; P. Papale for having calculated the fluid pressures; A. Neri for the assistance in diffusion calculations; M. D'Orazio for ICP-MS analyses of whole rock trace elements; A. Zanetti for SIMS analyses of melt inclusions; F. Colarieti for assistance during sample preparation, E.S. Waguena for sample preparation and help in FTIR measurements; P. Pantani for graphic assistance. This work was supported by Gruppo Nazionale per la Vulcanologia and Istituto Nazionale di Geofisica e Vulcanologia (Italy).

References

Allard, P., J. Carbonelle, N. Métrich, H. Loyer, and P. Zettwoog, Sulphur output and magma degassing budget of Stromboli volcano, *Nature*, *368*, 326–330, 1994.

Arai, S., An estimation of the least depleted spinel peridotite on the basis of olivine-spinel mantle array, *Neues Jahrb. Mineral. Monatsh.*, *8*, 347–354, 1987.

Barberi, F., M. Rosi, and A. Sodi, Volcanic hazard assessment at Stromboli based on review of historical data, *Acta Vulcanol.*, *3*, 173–187, 1993.

Bertagnini, A., M. Coltelli, P. Landi, M. Pompilio, and M. Rosi, Violent explosions yield new insights into dynamics of Stromboli volcano, *Eos Trans AGU*, *80*(52), 633, 636, 1999.

Bonaccorso, A., C. Cardaci, M. Coltelli, P. Del Carlo, S. Falsaperla, S. Panucci, M. Pompilio, and L. Villari, Annual report of the world volcanic eruptions in 1993, Stromboli, *Suppl. Bull. Volcanic Eruptions*, *35*, 8–14, 1996.

Bottazzi, P., L. Ottolini, R. Vannucci, and A. Zanetti, An accurate procedure for the quantification of rare earth elements in silicates, in *Secondary Ion Mass Spectrometry, SIMS IX Proceedings*, edited by A. Benninghoven et al., pp. 927–930, John Wiley, New York, 1994.

Carroll, M. R., and J. D. Webster, Solubilities of sulfur, noble gases, nitrogen, chlorine and fluorine in magmas, in *Volatiles in Magmas*, *Rev. Mineral.*, vol. 30, pp. 231–271, Mineral. Soc. of Am., Washington, D. C., 1994.

Carslaw, H. S., and J. C. Jaeger, *Conduction of Heat in Solids*, 510 pp., Clarendon, Oxford, U. K., 1959.

Coltelli, M., S. Falsaperla, P. Del Carlo, M. Pompilio, and A. Bonaccorso, Volcanic, seismic, and ground deformation data concerning the Stromboli volcano in 1995, *Suppl. Bull. Volcanic Eruptions*, *35*, 8–14, 1999.

Danyushevsky, L. V., N. Della Pasqua, and S. Sokolov, Re-equilibration of melt inclusions trapped by magnesian olivine phenocrysts from subduction-related magmas: Petrological implications, *Contrib. Mineral. Petrol.*, *138*, 68–83, 2000.

Danyushevsky, L. V., A. W. McNeil, and A. V. Sobolev, Experimental and petrological studies of melt inclusions in phenocrysts from mantle-derived magmas: An overview of techniques, advantages and complications, *Chem. Geol.*, *183*, 5–24, 2002.

Dixon, J. E., and V. Pan, Determination of the molar absorptivity of dissolved carbonate in basaltic glass, *Am. Mineral.*, *80*, 1339–1342, 1995.

Donaldson, C. H., Calculated diffusion coefficients and the growth rate of olivine in a basalt magma, *Lithos*, *8*, 163–174, 1975.

Francalanci, L., S. Tommasini, S. Conticelli, and G. R. Davies, Sr isotope evidence for short magma residence time for the 20th century at Stromboli volcano, Italy, *Earth Planet. Sci. Lett.*, *167*, 61–69, 1999.

Gerlach, T. M., H. R. Westrich, and R. B. Symonds, Preeruption vapor in magma of the climactic Mount Pinatubo eruption: Source of the giant stratospheric sulfur dioxide cloud, in *Fire and Mud: Eruptions and Lahars of Mount Pinatubo, Philippines*, edited by C. G. Newhall and R. S. Punongbayan, pp. 415–433, Univ. of Wash. Press, Seattle, 1996.

Ghiorso, M. S., and R. O. Sack, Chemical transfer in magmatic processes IV, *Contrib. Mineral. Petrol.*, *119*, 197–212, 1995.

Gurenko, A. A., T. H. Hansteen, and H. U. Schmincke, Evolution of parental magmas of Miocene shield basalts of Gran Canaria (Canary Islands): Constraints from crystal, melt and fluid inclusions in minerals, *Contrib. Mineral. Petrol.*, *124*, 422–435, 1996.

Jambon, A., P. Lussiez, R. Clocchiatti, J. Weisz, and J. Hernandez, Olivine growth rates in tholeiitic basalt: An experimental study of melt inclusions in plagioclase, *Chem. Geol.*, *96*, 277–287, 1992.

Jurewicz, A. J. C., and E. B. Watson, Cations in olivine, part 2: Diffusion in olivine xenocrysts, with applications to petrology and mineral physics, *Contrib. Mineral. Petrol.*, *99*, 186–201, 1988.

Kamenetsky, V., N. Métrich, and R. Cioni, Primary melts of Vulsini (Roman Province): Evidence from mineralogy and melt inclusions, *Contrib. Mineral. Petrol.*, *120*, 186–196, 1995.

Keppler, H., Experimental evidence for the source of excess sulfur in explosive eruptions, *Science*, *284*, 1652–1654, 1999.

Massare, D., N. Métrich, and R. Clocchiatti, High-temperature experiments on silicate melt inclusions in olivine at 1 atm: Inference on temperatures of homogenization and H_2O concentrations, *Chem. Geol.*, *183*, 87–98, 2002.

McDonough, W. F., and S. Sun, The composition of the Earth, *Chem. Geol.*, *120*, 223–253, 1995.

Métrich, N., A. Bertagnini, P. Landi, and M. Rosi, Crystallisation driven by decompression and water loss at Stromboli volcano (Aeolian Islands), *J. Petrol.*, *42*, 1471–1490, 2001.

Métrich, N., M. Bonnin-Mosbah, J. Susini, B. Menez, and L. Galoisy, Presence of sulfite (S^{IV}) in arc magmas: Implications for volcanic sulfur emissions, *Geophys. Res. Lett.*, *29*(11), 1538, doi:10.1029/2001GL014607, 2002.

Newman, S., and J. B. Lowenstern, 2002 VOLATILECALC: A silicate melt-H_2O-CO_2 solution model written in visual basic excel, *Comput. Geosci.*, *28*, 597–604, 2002.

Papale, P., Modelling of the solubility of two-component H_2O-CO_2 fluid in silicate liquids, *Am. Mineral.*, *84*, 477–492, 1999.

Peccerillo, A., and S. R. Taylor, Geochemistry of Eocene calc-alkaline volcanic rocks from Kastamonu area, northern Turkey, *Contrib. Mineral. Petrol.*, *58*, 63–81, 1976.

Roedder, E., Inclusion measurements: Heating, cooling, decrepitation and crushing, in *Fluid Inclusions*, *Rev. Mineral.*, vol. 12, edited by E. Roedder, pp. 181–221, Mineral. Soc. of Am., Washington, D. C., 1984.

Rosi, M., A. Bertagnini, and P. Landi, Onset of the persistent activity at Stromboli volcano (Italy), *Bull. Volcanol.*, *62*, 294–300, 2000.

Sato, H., Nickel content of basaltic magmas: Identification of primary magmas and a measure of the degree of olivine fractionation, *Lithos*, *10*, 112–120, 1977.

Scaillet, B., B. Clemente, M. W. Evans, and M. Pichavant, Redox control of sulfur degassing in silicic magmas, *J. Geophys. Res.*, *103*, 23,937–23,949, 1998.

Schiano, P., J. M. Eiler, I. D. Hutcheon, and E. M. Stolper, Primitive CaO-rich, silica undersaturated melts in island arcs: Evidence for the involvement of clinopyroxene-rich lithologies in the petrogenesis of arc magmas, *Geochem. Geophys. Geosyst.*, *1*, paper 1, 2000.

Tibaldi, A., Multiple sector collapses at Stromboli volcano, Italy: How they work, *Bull. Volcanol.*, *63*, 112–125, 2000.

Wallace, P. J., Volcanic SO_2 emissions and the abundance and distribution of exsolved gas in magma bodies, *J. Volcanol. Geotherm. Res.*, *108*, 85–106, 2001.

Zhang, Y., D. Walker, and C. E. Lesher, Diffusive crystal dissolution, *Contrib. Mineral. Petrol.*, *102*, 492–513, 1989.

A. Bertagnini and P. Landi, Istituto Nazionale di Geofisica e Vulcanologia, Sezione Roma I, sede di Pisa, Via della Faggiola 32, I-56126 Pisa, Italy. (bertagnini@pi.ingv.it)

N. Métrich, Laboratoire Pierre Süe, CEA-CNRS, CE-Saclay, F-91191 Gif/Yvette, France.

M. Rosi, Dipartimento di Scienze della Terra, Università degli Studi di Pisa, Via S. Maria 53, I-56126 Pisa, Italy.